

Alma Mater Studiorum Università di Bologna
Archivio istituzionale della ricerca

Characterisation of typical patinas simulating bronze corrosion in outdoor conditions

This is the final peer-reviewed author's accepted manuscript (postprint) of the following publication:

Published Version:

Masi, G., Esvan, J., Josse, C., Chiavari, C., Bernardi, E., Martini, C., et al. (2017). Characterisation of typical patinas simulating bronze corrosion in outdoor conditions. MATERIALS CHEMISTRY AND PHYSICS, 200, 308-321 [10.1016/j.matchemphys.2017.07.091].

Availability:

This version is available at: <https://hdl.handle.net/11585/609736> since: 2020-02-11

Published:

DOI: <http://doi.org/10.1016/j.matchemphys.2017.07.091>

Terms of use:

Some rights reserved. The terms and conditions for the reuse of this version of the manuscript are specified in the publishing policy. For all terms of use and more information see the publisher's website.

This item was downloaded from IRIS Università di Bologna (<https://cris.unibo.it/>).
When citing, please refer to the published version.

(Article begins on next page)

Characterisation of typical patinas simulating bronze corrosion in outdoor conditions

G. Masi^{a,*}, J. Esvan^b, C. Josse^c, C. Chiavari^d, E. Bernardi^e, C. Martini^f, M.C. Bignozzi^a, N. Gartner^g, T. Kosec^g, L. Robbiola^{h,*}

^a Dipartimento di Ingegneria Civile, Chimica, Ambientale e dei Materiali, Università di Bologna, via Terracini 28, 40131 Bologna (Italy) - giulia.masi5@unibo.it, maria.bignozzi@unibo.it

^b Centre Interuniversitaire de Recherche et d'Ingénierie des Matériaux, Université de Toulouse, 4 allée Emile Monso, 31030 Toulouse (France) - jerome.Esvan@ensiacet.fr

^c Centre de Microcaractérisation Raimond Castaing (CNRS UMS 3623), Université Fédérale de Toulouse, 31000 Toulouse (France) - claudie.josse@ensiacet.fr

^d Dipartimento di Beni Culturali, Università di Bologna, Italy - cristina.chiavari@unibo.it

^e Dipartimento di Chimica Industriale “Toso Montanari”, Università di Bologna, viale del Risorgimento 4, 40136 Bologna (Italy) - elena.bernardi@unibo.it

^f Dipartimento di Ingegneria Industriale, Università di Bologna, viale del Risorgimento 4, 40136 Bologna (Italy) - carla.martini@unibo.it

^g Slovenian National Building and Civil Engineering Institute, Dimičeva 11, SI-1000 Ljubljana, Slovenia - nina.gartner@zag.si, tadeja.kosec@zag.si

^h TRACES lab, CNRS (UMR5608), Université Toulouse Jean-Jaurès, 5, allées Antonio-Machado, 31058 Toulouse (France) - robbiola@univ-tlse2.fr

Abstract

In order to bring the treatment of historical bronze monuments in line with proper engineering practice and cultural heritage regulations, the standardisation of artificially aged surfaces that are comparable with natural ones is still to take place. In this aim, this investigation reports a comparative study of corroded quaternary bronze samples produced by accelerated ageing tests, simulating the unsheltered and sheltered exposure conditions mainly affecting outdoor bronze monuments. The effects of run off in a dropping test (unsheltered simulation) and the exposure to stagnant acid rain in a wet & dry test (sheltered simulation) on a bronze surface

* Corresponding authors:

Giulia Masi (Tel.: +39 051 2090361. e-mail address: giulia.masi5@unibo.it)

Luc Robbiola (Tel.: +33 0561 50 2435. e-mail address: robbiola@univ-tlse2.fr)

were studied. A multi-analytical approach was performed including conventional analytical methods, such as a microscopy examination coupled with elemental and structural analyses of the surface. In addition, a focused ion beam (FIB) was used to produce cross-sections in the size range up to a few tens of nanometres. It is evidenced that the corrosion layers, forming a nano-porous structure, are linked to a decuprification process marked by the preferential dissolution of Cu and Zn and the formation of a Sn-O species network within the barrier layer. A correlation between the tin content of the alloy and the corrosion amplitude is shown: the anodic areas are related to the lowest tin-content part of the alpha phase (in the centre of the dendrite), while the eutectoid areas (including the delta phase) are cathodic and therefore not attacked. The corroded samples artificially aged are well representative of natural corrosion structures observed on outdoor bronzes.

Keywords: bronze; artificial ageing; atmospheric corrosion; FIB; nano-porous corrosion layer.

Highlights

- Two artificial ageing processes well simulate outdoor patinas of as-cast bronze
- Distribution of chemical elements are detailed according to exposure conditions
- Surface characterization with *in situ* FIB cross-section highlights decuprification phenomenon
- Alpha (Cu) solid solution is anodic towards (alpha+delta) eutectoid
- Nano-porosities are evidenced within patinas according to corrosion process

1. Introduction

Artistic and historical bronze assets represent a large fraction of Europe's outdoor monuments. Copper and bronze surfaces are also very common in building infrastructures, industry and architecture (*e.g.*, copper roofs, facades, panels, bronze accessories like fences, doors, handles, pipes...). Currently, effective bronze protection remains a challenging question: more durable and efficient non-hazardous protective coatings (*e.g.*, without toxic benzotriazole) are required [1–3]. Moreover, a lack of understanding of the protection of bronze, taking into consideration not only environmental aggressiveness, but also the composition of the patinas, is frequently observed.

One of the challenges is to take into account the natural surfaces induced by corrosion in urban conditions, as the protective treatments are usually applied on oxidized bronze surfaces that display a different reactivity to metallic surfaces [4]. This requires the use of properly aged surfaces for applying and assessing appropriate conservation treatments, corresponding to the composition and structure of the natural corrosion layers. Another challenge is to develop new protocols for the preparation of surfaces and the application of protective coatings in order to modify conservation treatments to meet international standards and engineering practice, which also involves the standardization of controlled surfaces.

In most cases, the assessment of coatings or of the corrosion inhibitors has been performed on bare metallic surfaces. Pure Cu-containing compounds were applied or electrochemically produced on the bronze surface to simulate real natural patinas [5,6]. However, artificial patination based only on the deposition of Cu-based compounds is insufficient to reproduce the complexity of natural patinas.

In fact natural bronze outdoor patinas, which are the real substrates for protective treatments, were shown to have different characteristics depending on the exposure conditions, mainly related to sheltered or unsheltered areas [7–9]. These characteristics are linked to the selective dissolution of the copper ions of the bronze, which in the case of sheltered areas can precipitate out, forming an external deposit of copper hydroxysulphate species, while for unsheltered areas a more complex process is involved [7–9]. In particular, in urban atmospheres, patinas directly exposed to rain are unstable and are cyclically leachable by rainwaters. This is usually revealed by the green streaks on stone basements after several decades. It is characterized by a selective enrichment of tin-containing species within the patinas, forming nanoclusters and partially amorphous compounds, not detected by usual methods such as X-ray diffraction, but clearly evidenced by transmission electron microscopy

[8]. This phenomenon of selective copper dissolution is commonly found on bronze monuments, regardless of their composition and age [9,10].

In order to develop effective protection strategies, better understanding of the corrosion process on ancient materials was recently developed from specifically adapted ageing tests. In particular, the impact of artificial acid solutions used for simulated natural rainwaters highlighted the behaviour of alloying elements that release in different ways from the bronze surface, revealing the absence of dissolved tin [11,12]. In this context, an approach based on two specific exposure conditions has been set up on artificial quaternary bronze coupons exposed to synthetic rain, with a monitored time of wetness (ToW) [12,13]. For simulating the effect of run off (typical of the unsheltered parts of outdoor monuments), the rainfall is replicated by periodically dropping acid rain onto a surface coupon (Dropping test) [12]. On the other hand, for replicating the ageing conditions typical of sheltered areas, the action of stagnant water is reproduced by alternating immersions inducing wet and dry cycles (W&D test) [13]. Very similar features are found for patinas produced by these artificial ageing methods and for natural patinas [8]. This global procedure is a further advancement for developing testing procedures and new protective treatments, overcoming the difficulties of simulating natural bronze patinas formed upon exposure to outdoor atmospheric environments.

In fact, the application of these ageing tests appears to be a good way to form reproducible, artificially aged patinas. So the present study aims to strengthen this approach by producing an implemented surface-patination system and a characterization protocol. It was applied to achieve a batch of artificially aged samples obtained using the “dropping” test and the W&D test. Some technical features were developed in order to optimize the scale-up of the dropping system. In this study, we focused on the surface characterisation of artificially aged patinas produced on a typical Cu-Sn-Zn-Pb cast bronze. Here, the alloy composition exhibits a higher tin content than that previously used for initially testing the procedure [12,13]. Specific attention is paid also to poorly developed patinas simulating very thin corrosion layers in accordance with regulated engineering practices and in line with cultural heritage practice. The alloy composition of bronze monuments can exhibit a large variation of the contents of alloying elements [14]. However, it is always linked to only two different metallurgical states, as lead is not miscible in copper alloys. It is either related to a single alpha copper solid solution alloy or, as investigated in this work, to a biphasic one additionally including the alpha and delta ($\text{Cu}_{41}\text{Sn}_{11}$) eutectoid.

The aim of this work was to study the difference between corroded quaternary bronze samples produced by accelerated ageing tests simulating sheltered and unsheltered atmospheric exposure conditions on outdoor bronze monuments. The comparison between these two types of aged surfaces was performed by applying a set of complementary tools. Conventional investigation methods, such as optical (OM) and scanning electron (SEM) microscopy, were applied, combining an elemental (EDS) and structural investigation, both on the outermost surfaces (XPS) and on the deeper layers (Raman micro-spectroscopy and X-ray diffraction (XRD)). These methods were complemented by focused ion beam (FIB) milling for the preparation of cross-sections, which were observed with a field-emission-gun (FEG) SEM/EDS at a resolution scale of a few nm. Special attention was paid to correlating the surface and cross-section information.

2. Experimental Methods

2.1 Artificial rain and ageing methods

The artificially corroded bronze samples were produced by applying two different accelerated ageing methods: the “dropping” method, simulating unsheltered areas, and the wet & dry (W&D) method, simulating sheltered conditions in atmospheric exposure. Before the patination the quaternary bronze coupons ($50 \times 25 \text{ mm}^2$) were polished with abrasive SiC papers up to Fepa P 1000 grit, degreased by acetone and rinsed with distilled water.

The artificial rain solution, used in both the ageing tests, was prepared according to the composition of natural acid rains collected during the winter months in Bologna [13]. The ion concentrations of the weathering solution were SO_4^{2-} 1.90 mg L^{-1} , Cl^- 1.27 mg L^{-1} , NO_3^- 4.62 mg L^{-1} , CH_3COO^- 0.23 mg L^{-1} , HCOO^- 0.05 mg L^{-1} , NH_4^+ 1.05 mg L^{-1} , Ca^{2+} 0.34 mg L^{-1} , Na^+ 0.53 mg L^{-1} , with a measured pH of 4.35.

In this study, the dropping test for reproducing the main features of natural patinas in unsheltered areas was specifically adapted to produce a large set of corroded samples. This test has been improved from the one previously used in [12] and [15]: similarly to the set up used in [15] the largest aged areas have been provided by splitting the rain flux dropping on each sample into four drops, but a higher number of samples has been obtained at the same time. Figure 1 shows a schematic of the unit in which two water pumps for each line distributed the weathering solution on the bronze coupons. In this study, two dropping units were applied and 52 bronze samples were aged in the same batch. Artificial rain was guttered

in four drops over the samples, inclined at 45°, with an average drop height of 3.5 cm and an average dropping rate per sample of 270 cm³/h; 12 h of dropping was continuously alternated with 12 h of dry phase until a total ToW of 37 days was completed. In order to ensure a constant dropping rate for each sample, a rotation of 180° for each sample during the dropping test was made every day.

Figure 1: (a) Schematic mode for a large-scale production of dropping test samples and (b) general view of the dropping system; (c) detail showing the quaternary bronze samples (at 45°) during ageing exposed at 45°.

The W&D test conditions are described in detail in [13], except for the larger size of the bronze samples used (50 × 50 mm² instead of 50 × 25mm² here). A one-hour cycle was made up of a wetness period of 20 min and a dry period of 40 min in order to reproduce the main features of the natural patinas in sheltered areas of outdoor bronze monuments. Considering 20 min for the sample to get dry, a ToW of 40 min is assumed to correspond to an hourly cycle and the W&D test was run until a total ToW of 87 days was completed. The weathering solution, 350 mL per cell (pH of 4.35), was renewed twice a week when the pH became neutral.

2.2 Bronze alloy

The type of bronze employed for this study as the substrate for the production of artificial patinas is a quaternary cast Cu-Sn-Zn-Pb alloy. It was selected in accordance with the composition of the last centuries bronzes commonly used for sculptures by the art foundries and always used up to nowadays [10,14]. Its elemental composition is (wt%): 6.9±0.6 Sn, 3.1±0.4 Zn, 2.0±0.9 Pb also containing Al, P, Mn and Si in traces (Cu to balance). This corresponds to (at%): 3.9 Sn, 3.2 Zn and 0.6 Pb. The Cu/Sn atomic ratio is about 23.6. It has been used in the as-cast condition (thickness of about 5 mm). Cast Cu-based alloys are sensitive to coring, inducing micro- but also macro-segregation of the alloying elements [16]. The local variations in the concentration of tin and zinc, soluble in the Cu solid solution, are related to this usual behaviour of traditional bronze during casting. For lead, this large variation has to be ascribed to Pb globules that are not miscible in the Cu matrix. The microstructure of the bronze alloy is dendritic, typical of cast bronzes. The dendrites are several hundred microns in length, which corresponds to slow cooling, as usually observed on traditional bronze obtained from sand casting. As shown in Figure 2 a-b, the large network of dendrites includes shrinkage porosities.

Figure 2: Optical examination of as-cast quaternary alloy before corrosion (tint etchant Klemm III): (a) as-cast alloy with large dendritic structure (mm size); (b) cross-section with vertical preferential orientation of the dendrites linked to cooling temperature gradient from the top surface to the plate centre; corroded surfaces obtained by dropping (D) and by wet & dry (W&D); (c-d) Optical bright-field observation and (e-f) 3-D digital microscopy topographic images of bronze samples after artificial corrosion by the dropping and W&D tests, respectively.

2.3 Surface analysis and structural characterization

The artificially aged bronze samples were first observed under an optical microscope and a scanning electron microscope, coupled with X-ray energy-dispersive spectroscopy (low vacuum LEO LV 435 coupled to a PGT IMIX system with a Ge detector). Measurements were performed at 15 KeV with a current beam intensity of 1.5 nA, using certified standards for quantification.

X-ray Diffraction (XRD) was also performed using a DRX D8 Advance (Bruker) apparatus (Cu-K α , $\lambda = 0.15418$ nm) with a fast detector (LynxEye). The samples were analysed in grazing-incidence mode (GXR) to better analyse the thin corrosion layer (incident angle fixed at 1°, pattern acquisition from 10° to 80°, 2 θ , step of 0.03° and step time of 24 s) on a surface area of ~0.5 cm².

Raman spectroscopy was performed in order to determine the composition of the surface species at the micro-level, in addition to the X-ray diffraction performed on a larger surface scale. Measurements were carried out on the artificially aged quaternary bronze surfaces with a Horiba Jobin Yvon LabRAM HR 800 apparatus (grading resolution of 600 lines/mm, excitation wavelength 532.0 nm (Ar diode), with an Olympus objective $\times 100$ (NO 0.9) allowing a theoretical lateral resolution of 0.7 μm at a maximum depth of 2.61 μm). The alignment was calibrated for the first order of a pure Si crystal (520.7 ± 1 cm⁻¹). The scan number and the accumulation time (usually 60 s) were adapted according to the intrinsic signal intensity (specifically here, 30 s \times 3 acquisition, at an energy < 5 mW). The acquisition and treatments of the spectra were performed with LabSpec software.

XPS analyses were carried out on the artificially patinated surfaces using a monochromated Al-K α source ($h\nu = 1486.6$ eV) on a ThermoScientific K-Alpha system. The X-ray spot size was about 400 μm in diameter. The photoelectron emission spectra were recorded with a pass energy fixed at 130 eV with a step of 1 eV for surveys, and pass energy of 40 eV with a step of 0.1 eV for core levels. Ionic sputtering of the surfaces was made with an Ar⁺ ion beam accelerated under 200 eV and a low current for 30 s. A smart method was used for the

background subtraction. The XPS analysis depth is only limited to the first atomic layers (a few nm).

Cross-sections of bronze samples, previously analysed by SEM/EDS, XRD and XPS, were also investigated after applying the focused ion beam (FIB) apparatus (FEI Helios NanoLab 600i). The FIB uses Ga^+ ions to remove material with a very high spatial precision. In this way cross-sections can be made at a specific location after surface observation and representative sampling area. For this operation, the sample is positioned in the SEM chamber, tilted at 52° , and a platinum (Pt) layer of 2- μm thickness is first laid down for surface protection. Then FIB milling is then applied to etch the sample. In particular, corroded dendrites surrounded by a eutectoid were selected as typical areas of interest for the FIB cross-sections of quaternary bronze. The FEG-SEM imaging, X-ray maps and line-scans (Aztec Oxford system with SSD detector, WD 4mm) were performed using different applied energies of electrons (10 KeV and 15 KeV) in order to detect all possible elements. Under these conditions, the X-ray emission depth for the O $\text{K}\alpha$ (0.53 keV), Cu $\text{L}\alpha_1$ (0.93 keV) and Zn $\text{L}\alpha_1$ (1.01 keV) lines is roughly of the order of 100 nm, while it is at least twice as much for Sn $\text{L}\alpha_1$ (3.44 keV). Thus, the X-ray intensity values of the X-ray maps and the line-scans obtained for these elements are related to different analysed volumes.

3. Results and discussion

3.1 Surface observation and elemental analysis

Optical observations of the bronze samples, artificially aged by dropping and W&D tests, are reported in Figure 2c and d, respectively. Artificial ageing highlighted the typical dendritic structure of the as-cast bronze alloy.

The corrosion attack is not uniform and more deeply affects the Cu-rich centre part of the dendrites: black for dropping (Figure 2c) and reddish for W&D (Figure 2d). The interdendritic areas with eutectoid, corresponding to the bright gold surfaces, are less modified by the corrosion attack than the dendrite core. The two ageing systems, however, induced different surface morphologies, as revealed by the 3D digital microscopy topographic images. For dropping (Figure 2e), due to the run off of acid rain, a slight erosion ($\sim 1\ \mu\text{m}$) of the central part of the dendrite is revealed. For W&D (Figure 2f), the presence of a deposit of corrosion compounds is found on the dendrites, inducing a slight increase of the thickness ($< 1\ \mu\text{m}$) and an increased roughness by comparison with the original surface.

Detailed observations by SEM-BSE are shown in Figure 3. In both ageing tests (Figures 3a and d), the corroded dendrites (in dark grey) are surrounded by the inter-dendritic region, which includes the eutectoid (in light grey) but also black spots, which represent porosities due to solidification shrinkage during casting. It is confirmed that the corrosion attack is heterogeneous: α -Cu solid solution with an initially lower Sn content is more severely corroded, whereas the dendrite borders with a higher tin content and the (α + δ) eutectoid (white area) are not attacked by corrosion. This is confirmed from elemental characterisation carried out by EDS coupled with SEM.

Figure 3: SEM observation and X-ray intensity maps of surface aged by dropping (a-c) and W&D (d-f): (a) and (d) BSE images; (b) and (e) Composite X-ray map image (O in green, Cu in magenta and Sn in blue) showing that the corrosion mainly affects the dendrite centre; (c) Composite X-ray map image (Cl in green and Cu in red) revealing a higher Cl concentration in the centre of corroded dendrite; (f) Composite X-ray map image (S in red and Cl in green) showing a large amount of S in the dendrite linked to the corrosion deposit.

The composite images relative to the X-ray emission of O K (red), Cu K (green) Sn L (blue) signals are reported in Figures 3b and e for dropping and W&D, respectively. The eutectoid (in light blue) and dendrite borders (in blue-green) are poorly attacked (no or a very low O signal detected). In contrast, the corroded dendrite areas can be observed by the high O and low Cu emissions, defining two main areas: purple (blue + red) in the external part (high Sn emission) and yellow in the central part (low Sn emission). For both ageing tests, this result highlights the substantial Cu dissolution relative to the tin content in the alloy, according to the preferential dissolution of Cu. However, a different behaviour within the corroded dendrites was observed, depending on the exposure conditions. For dropping, as shown in Figure 3c, Cl (in green) is locally observed in very small amount in the centre of the dendrites. It is also related to a more important Cu emission (in yellow in Figure 3b). For W&D, as shown in Figure 3f, both Cl and S are detected in small amounts all over the corroded areas: Cl (in green) mainly in the centre of the dendrites, but also S (in red) more to the edge of the corroded dendritic parts. For W&D, this has to be related to the incorporation of S- and Cl-containing compounds within the corrosion deposit, previously evidenced in Figure 1b.

Elemental quantification of the different surface regions of the dendrites was performed on the basis of EDS analyses. The results are reported in at% in Table 1. Adjacent to the eutectoid, the dendrite borders exhibit a comparable chemical composition between the two samples. Zinc is clearly detected, while the Sn content is, as expected, close to the limit of

solubility of the α -Cu solid-solution atomic ratio (Cu/Sn \sim 12). However, oxygen is detected in a small amount: the dendrite borders are weakly attacked and are covered by a thin corrosion layer.

Table 1: Chemical composition of quaternary bronze artificially patinated through dropping and W&D (EDS – Beam energy 15 kV). The reported results are an average obtained from different areas.

In the corroded parts of the dendrites, the main differences between all the areas, previously highlighted by X-ray maps, are linked to the variation of the Cu content. For both ageing methods, a trend in the chemical composition is observed. It is confirmed that a small quantity of environmental elements (Cl and S) were detected, but in larger amounts for the W&D.

In fact, the differences between these corroded areas are mainly linked to Cu dissolution coupled to the relative Sn enrichment. Interestingly (Table 1), the Cu/Sn ratio is markedly higher within the centre of the corroded dendrites. This can be related to the deposition of the Cu species, but it can also be linked to the initially low Sn concentration in the centre of the dendrites due to casting, as shown later. The results reported in Table 1 also confirm that the aged surfaces obtained by the dropping method exhibit lower Cu/Sn ratios compared to the surface aged by W&D, in good agreement with previous results [12,13]. In fact, the combined chemical–mechanical action induced by the dropping method generated a higher Cu dissolution rate and limited the growth of Cu deposits in comparison to the W&D procedure.

A low Zn content was observed in all the corroded areas due to its preferential dissolution in bronze, as already reported [8,11]. For Pb, a significant amount was detected on the surfaces aged by W&D, whereas only traces were detected in the dropped surface. In the case of W&D, the Sn/Pb atomic ratio is found to be almost constant at around 10 for all of the analysed areas. This is probably due to the tetravalent nature of Pb, that spread all over the surface and easily formed compounds with environmental elements within the corrosion layer [17].

Thus, these results confirm that the artificial ageing induced corrosion with surface oxidation, forming a thin corrosion layer. This patinated structure will be assimilated into thin natural patina, representative of its initial formation, according to their detailed composition and structure, as described below.

3.2 Structural characterization

3.2.1 X-ray diffraction and Raman spectroscopy

The X-ray diffraction patterns performed on large surface area (around 0.5 cm²) at low diffraction angles for artificially patinated surfaces are shown in Figures 4a and b, respectively, for the dropping and W&D tests. In addition to the Cu solid solution, cuprous oxide (Cu₂O) was also identified for both ageing tests. Moreover, the surface aged by W&D (Figure 4b) also revealed posnjakite, a Cu hydrated hydroxysulphate (Cu₄(OH)₆SO₄·H₂O). This compound is a precursor of brochantite, which forms for longer exposure times on copper [17,18]. This behaviour confirms the difficulty of forming stable corrosion compounds for the dropping system due to the run-off regime at the surface.

Figure 4: Grazing-angle X-ray diffraction (GXRD) of the corroded surface by (a) dropping and (b) W&D; Raman spectroscopy performed on corroded dendrite of artificial quaternary bronze patinated surface by (c) dropping (top spectrum: metal-O stretching vibration / bottom spectrum: cuprous oxide) and by (d) W&D (top: posnjakite / bottom: cuprous oxide).

The X-ray diffraction analyses performed on large surface areas were completed at a micrometric level by applying Raman spectroscopy. Even though Raman spectroscopy is a very sensitive method for the characterization of oxidized metallic surfaces, processing the spectra was rather difficult, mainly due to the very low thickness and due to the poor crystallisation of the surface compounds.

Typical spectra of the identified compounds by Raman spectroscopy are reported in Figures 4c and d. The phase-composition determination of the aged surfaces using the dropping or W&D tests proved to be rather different.

For the dropping tests, unlike for the W&D, Raman spectroscopy measurements gave poorly resolved signals. Raman spectroscopy performed on different areas of the corroded surface confirmed the formation of cuprous oxide (Figure 4c, bottom spectrum). In this spectrum a doublet at 293–343 cm⁻¹ was also observed. It is difficult to ascribe, but it could correspond to the M-O stretching vibration, such as for CuO (305–350 cm⁻¹), and not expected here. The black spectrum in Figure 4c (top) exhibits intense, but very broad, peaks at 531 and 600 cm⁻¹, characteristic of M-O stretching vibrations, probably indicating the presence of several compounds mixed together, which could be related to Cu but also to Cu and/or Sn oxides [19–22]. In this spectrum, the peak at 218 cm⁻¹ indicates the presence of Cu₂O, marked by a large band in the 1100–1230 cm⁻¹ region. A characteristic Raman fingerprint is the 272–323 cm⁻¹ doublet linked to the peaks in the 600–200 cm⁻¹ region. These fingerprints do not exactly correspond to the pure cuprite (Cu₂O), tenorite (CuO) and chalcocite (Cu₂S), but could be

compatible with a mixture of these Cu-containing phases [22]. Furthermore, the attribution of the strong $\sim 530\text{ cm}^{-1}$ peaks forming a broad structure associated with weak bands at ~ 750 and 777 cm^{-1} (Figure 4c, top spectrum) does not correspond to the cassiterite fingerprint. This result could be linked to a non-stoichiometric tin oxide, probably hydrated, which could correspond to the SnO_{2-x} or substituted Sn(M)O_2 oxide (where M is a bronze alloying element) but also hydroxyl tin oxide [19,21,22].

For the W&D tests, two compounds were punctually identified by Raman spectroscopy, fully confirming the X-ray diffraction measurements: cuprous oxide and posnjakite. In Figure 4d, the spectrum of cuprous oxide Cu_2O (bottom spectrum in blue) exhibits the characteristic features of well-crystallised compounds marked by the $215\text{--}220\text{ cm}^{-1}$ and $620\text{--}630\text{ cm}^{-1}$ peaks [20–22]. It should be noted that the poorly resolved cuprous oxide was also detected in the border of the dendrites, forming a thin corrosion film, as later confirmed from the FIB SEM observations. The spectrum on the top of Figure 4d corresponds to posnjakite [20], small, green-blue crystallites, localized in the centre of the dendrites. The stretching of the hydroxyl units in the posnjakite produced bands in the $3600\text{--}3300\text{ cm}^{-1}$ region. The sulphate group stretched symmetrically at 974 cm^{-1} , while the $600\text{--}200\text{ cm}^{-1}$ region with the 445 cm^{-1} peak is typical of Cu-O stretching. No evidence of tin-containing compounds was found for the W&D sample. This could be attributed to the fact that the tin oxide species could be non-stoichiometric, but also hydrated, and could be hindered by the higher Raman signals relative to the deposit of crystalline Cu species.

These results confirmed the differences in the main features of the surfaces aged with these two methods, previously highlighted by SEM and EDS analyses. Dropping allows the formation of poorly crystallised tin compounds (the top Raman spectrum in Figure 4c), related to selective Cu dissolution. For W&D, the alternate immersion action leads to the formation of thin corrosion layers of cuprous oxide with Cu sulphate corrosion products. It should be noted that chlorides, nitrates and carbonates were not detected.

3.2.2 XPS investigation

In order to define more precisely the top corrosion layers that can interact with the protective coating, XPS analyses were carried out on the artificially patinated surfaces. Figure 5 shows XPS surveys of the corroded surfaces before (in black) and after (in grey) Ar^+ -ion sputtering (30 s with Ar^+ ions accelerated to 200 eV).

Compared with the EDS analysis (Table 1), no Cl peaks on both the samples and no Zn on the W&D aged surface were found, indicating that chlorides (Cl element) is located in the inner part of the corrosion layers (hence non-detectable by XPS) and Zn is fully dissolved out of the top layer of the surface aged by W&D.

The short and slight etching applied here is very effective for these surface compounds. As shown in Figure 5, it allowed surface cleaning with respect to carbon contamination (C 1s peak decreasing), enhancing the global XPS signals of the main elements (O 1s, Zn 2p in the surface aged by dropping, Sn 3d and Pb 4f). Only the Cu 2p and S 2p exhibited a few changes. Specifically, the Cu 2p spectrum shows typical shake-up satellites before etching, which significantly decrease in intensity after ion sputtering, enhancing the main Cu 2p peaks at lower BE. Regarding S 2p, new contributions at lower BE are observed when the corroded surfaces were etched. This indicates Cu 2p and S 2p reduction under Ar⁺ sputtering, as reported in [23].

Figure 5: XPS surveys of the corroded surfaces by dropping and W&D before and after Ar⁺ ion etching.

The O 1s, Cu 2p core levels and the S 2p curve-fitted regions of the surfaces aged by the dropping (in black) and W&D (in grey) tests showed a similar behaviour (Figure 6). The main Cu 2p peaks are observed at BE=933.3 eV (Cu 2p_{3/2}, α'=1848.4 eV), probably due to a mix of Cu oxides. Other contributions were detected at about 935.0 eV (BE); they can be ascribed to Cu (II) hydroxyl-species [23–26]. Also, the O 1s core level showed a broad peak, with similar features between the two samples. An O 1s deconvolution was not performed, due to the presence of several contributions in the range of a few eV, which could correspond to different metal oxides and hydroxyl species. The main differences between the two samples are related to the S 2p signals (Figure 6e and f). In particular, for both the samples two S 2p contributions were detected: S 2p_{3/2} BE = 168.5 eV, ascribed to sulphates, and S 2p_{3/2} = 163.0 eV, attributed to the S-metal bond, also linked to etching effects [23,25,26]. However, for the dropping test, the S 2p signal is characterized by a low intensity and a high signal noise, confirming the EDS results. This might not just be related to Cu, but also to the minor amount of Pb(II) [26].

On the top surface, all the other metallic elements in smaller contents, Sn 3d, Zn 2p and Pb 4f, formed mostly oxides and/or hydroxides. As such, the environment of the different Cu 2p oxidation states for the dropped samples is mainly oxides and hydroxides, whereas, added to this for W&D surfaces, the S is mainly linked to Cu-developing hydroxysulphates.

Figure 6: XPS core levels of O 1s, Cu 2p and S 2p curve fitted regions, after Ar⁺-ion etching, on the bronze surface corroded by dropping (a, c and e, respectively) and W&D (b, d, f, respectively).

Table 2 reports the atomic quantification of an artificially patinated surface using the dropping and W&D tests for the main alloying elements as well as for C 1s, O 1s and S 2p.

Table 2: XPS atomic quantification on corroded surface by Dropping and W&D before and after Ar⁺-ion etching.

On the top surface corroded by dropping, not only Cu compounds are present. The concentrations of Sn 3d_{5/2}, Pb 4f_{7/2} and Zn 2p_{3/2} are higher compared to the W&D aged surfaces, coupled with a higher oxygen content. The Sn is present as Sn(IV), probably as tin oxides or hydroxides, but the broad and poorly resolved Sn LMM Auger at around 1053 eV cannot aid in further refinement of Sn spectrum interpretation. These observations confirm the difficulty of forming Cu-based corrosion deposits, due to the run off during the dropping tests. Conversely, on the W&D-aged surface, the Sn, Pb and Zn are almost completely absent. The surface is essentially covered with Cu compounds, mainly hydroxysulfates, but also oxides and a S-metal bond (after ion sputtering). In particular, the Cu 2p_{3/2} concentration (at%) is in almost the same ratio as the S 2p sulphate, indicating that nearly all the sulphates are bonded to Cu, in agreement with the detection of posnjakite by GXRD and the Raman spectroscopy results.

3.3 Cross-section analysis

Relationships between the surface corrosion and the bulk bronze alloy were investigated by FIB analysis. Typical areas of interest were selected in order to obtain a representative section of both the centre of a corroded dendrite and the adjacent inter-dendritic space (Figure 7a and b for the dropping and W&D samples, respectively). The corresponding FIB cross-sections are shown in Figures 7c and d.

Figure 7: Images of the corroded surface and cross-sections prepared by FIB milling of samples obtained by Dropping and W&D: (a) and (b) surface areas corresponding to cross-section obtained by FIB milling; (c) and (d) general views of the cross-section after FIB milling (rectangles are corresponding to details shown in Figure 8).

According to the previous reported results, the dendrites are more corroded than the dendrite borders, which are poorly attacked and the eutectoid is not corroded at all, as detailed in Figure 8.

Figure 8: Cross-sections prepared by FIB milling of samples obtained by dropping and W&D, corresponding to areas defined in Figure 7c-d: (A) dendrite centre, (B) dendrite borders corresponding to the transition corroded dendrite / eutectoid area and (C) interdendritic space (eutectoid).

Figures 7c and 7d provide a detailed view of the most corroded parts corresponding to the dendrites, characterised by a low tin content in comparison to the interdendritic spaces with here also contain the high tin content stable delta phase ($\text{Cu}_{41}\text{Sn}_{11}$). Different corrosion structures between the dropping and W&D samples are revealed: thicker for the dropping samples and thinner for the W&D samples, with a diverse distribution of nano-porosities. In particular, for the dropping samples (Figures 7c and 8A), the corrosion of the dendrites is uniform with a homogeneous thickness (about 2 μm), while for the W&D samples (Figures 7d and 8C), the corrosion layer is irregular and thinner: less than 1 μm in the dendrite core, and up to 2 μm close to the border parts. For W&D, this could be linked to the lateral junction of several localized attacks. In addition, for the dropping sample (Figure 8A) nano-porosities of a few tens of nm are observed throughout the whole corrosion layer. For the W&D sample (Figure 8B), the nano-porosities are essentially observed only in the outermost part of the layer.

A detailed view of the nano-porosities is shown in Figure 9. It is important to mention that the porous structure shown here was hypothesised for several years for bronze patinas formed in natural environments [8,9,27]. In fact, according to the process of decuprification leading to an internal oxidation of the alloy, it was found that the selective release of copper ions and the formation of patinas involved the presence of a porous structure, through which cations migrate outwards from the alloy to the corrosive environment, while the anions migrate inwards [27]. This fundamental point of the presence of a nano-porous structure is revealed thanks to the nm spatial resolution achieved using the FIB FEG-SEM technique. It has to be coupled to nano-precipitates of the tin-containing species (tin hydroxyl- and/or hydrated tin oxides) forming a stabilizing network within the corrosion structure. Thus, for both ageing tests, the main corrosion process involved is relative to the decuprification of bronze, like that observed for natural patinas. As also revealed in the EDS maps hereafter, it corresponds well to an internal oxidation of the alloy, with a preferential release of Cu ions (including also Zn) and marked by the formation of tin-insoluble species within a corrosion layer.

Figure 9: High-magnification observation of the corrosion layer revealing the porosity of bronze patinas on a nanometre scale obtained with FIB cross-sections of (a) the dropping and (b) the W&D samples.

As regards the nano-porosity distribution within the corroded dendrite (Figure 9), a difference appears between the dropping and W&D samples. This has to be related directly to the ageing process applied. In fact, for the dropping test, the dendrites are attacked more severely due to the permanent leaching of the alloy, inducing a permanent release of the Cu and Zn ions in relation to the internal oxidation. As a consequence, the developed network of nano-porosities has to be related to the formation of a porous barrier layer that is more pronounced for the dropping than for the W&D samples. In fact, for W&D samples, the corrosion is less developed and a more efficient barrier layer can be built up, limiting the alloy dissolution, the species migration throughout the layer and then consequently the nano-porosity network.

As previously pointed out through surface images, corrosion mainly affects the central part of the dendrites. Thus as revealed in Figure 8C for both samples, a marked transition between the centre and the border of the dendrites is revealed: the dendrite borders are poorly attacked and a corrosion film of a few tens of nm is emphasised. Investigations to identify this abrupt transition were carried out by recording EDS line-scans within the alloy, parallel to the surface. Representative X-ray profiles of the alloying elements in the W&D sample are shown in Figure 10, where the profiles are centred relative to the corroded dendrite.

A strong relationship between the Sn content in the alloy and the corrosion morphology was observed, validating the previous surface-characterisation results. As shown in Figure 10, the marked transition between the highly corroded core and the relatively unaltered border of the dendrites is linked to the transition from lower to higher Sn contents in the alloy, respectively, due to the Sn micro-segregation during cooling in the casting procedure. In particular, corrosion preferentially affects the dendrite areas with lower Sn contents (i.e., the core): an effect of galvanic coupling, linked to Sn segregation between the core of dendrites (anodic) and the border (cathodic), is clearly revealed from the observation of the cross-sections.

Figure 10: Representative EDS line-scan profiles of the quaternary alloy, located on the bulk alloy parallel to the corrosion layer and centred on the corroded dendrite.

Within the corroded dendrites, the corrosion process induced a preferential Cu and Zn dissolution linked to the presence of O element within the whole thickness of the corroded layer. This is shown by elemental X-ray maps within the corrosion layer (1 μm) obtained from the W&D tests (Figure 11). Furthermore, for the W&D tests, the distribution of S is not reported due to its very low emission signal. Also, small amounts of Cl were detected, but

only in the internal part of the corrosion layer, confirming the EDS results in Table 1 (surface analysis,) but also the XPS results, in which Cl was not detected on the top surface.

Figure 11: X-ray maps of the corrosion layer produced by W&D test in the centre of dendrite obtained by FIB cross-section (A right-hand image of Figure 8).

For a better understanding of the elemental distribution within the corrosion layers, EDS line-scans were performed vertically through the corrosion layers produced by the two ageing methods, as shown Figure 12 a-c. For the thick corrosion layers, the EDS profiles (Figure 12a and b) show a similar trend for Cu, Zn, O and Sn, characterised by a decrease of Cu and Zn within the corrosion and a relatively high and constant amount of O and Sn. For the very thin corroded layer (< 200 nm) reported in Figure 12c, only O, Cu and Sn were detected (the Zn signal was not resolved, so it is not reported). Also in this case, the corrosion features are comparable to the previously described thicker layer. In particular, a homogeneous decrease in the Cu signal coupled with the presence of O and a slight increase in Sn is shown, in accordance with the previous observation in Figures 12a and 12b. Thus, the preferential dissolution of Cu and Zn coupled with a relative Sn enrichment (decuprification) is confirmed, not only for the thickest corrosion layers, but also for the film of a few hundred nanometres.

For both aged surfaces, the S signal was very low and no information can be reported. In particular for the W&D outer layer, no S element (such as in posnjakite) was detected in the cross-section, in contrast to the surface analysis. This is probably due to the non-uniform distribution on the W&D surface.

As regards Cl element, a different behaviour is highlighted between the dropping and the W&D samples, but only for thick corrosion layers. Within the 2- μ m-thick dropping corrosion layer (Figure 12a), the presence of the chlorine content seems linked to a compact compound within the porous layer. For the W&D samples (Figure 12b), an enrichment of Cl is found at the corrosion/bronze interface, as a typical consequence of the selective action of this anion on anodic zones (the core of the dendrites) during the corrosion attack.

Figure 12: Elemental line profiles (X-ray intensity vs distance) obtained by cross-section prepared by FIB milling within the corrosion layer produced by dropping: (a) centre of corroded dendrite, and by W&D: (b) thicker part of the corroded dendrite and (c) thin layer in the dendrite border.

This confirms the specific role of Cl anions in the corrosion process of bronze in the presence of a cuprous oxide membrane, as already pointed out for other natural environments [27]. In particular, Cl anions can act either as “passive” anions, not directly involved in the

corrosion mechanism [28] (included in stable corrosion compounds within the layer as for the dropping samples), or the Cl^- can act as an “active” anion, directly involved in the corrosion process in relation with cuprous oxide layer, as revealed by their enrichment at the corrosion layer/alloy interface of the W&D sample.

3.4 Validation of representative ageing tests

Coupling the surface and cross-section analyses, two different behaviours were observed, in agreement with the previous studies, also performed on as-cast bronze exposed to accelerated ageing [12,13], taking into consideration the two main rainfall-exposure conditions (sheltered and unsheltered areas).

The dropping method induced a uniform porous layer, characterized by open pores with dimensions from a few nm up to tens of nm. On the other hand, the corrosion induced by the W&D was found to be less pronounced, as revealed by the smaller corrosion thickness, exhibiting an internal compact layer and a porous external one, marked by external corrosion deposits. Furthermore, a similar general corrosion behaviour was observed: the Cu and Zn dissolution, coupled with Sn enrichment, was highlighted and the corrosion layers mainly contained Cu, Sn compounds with a high O content. Pb is present in small amounts on the corroded surfaces and the Pb compounds were not clearly detected by XRD and Raman spectroscopy, as in [12,13]. Regarding the environmental elements, Cl was found in the inner part of the corrosion layer in both samples, but it is present in small amounts and as anions where the corrosion is more severe, not forming specific compounds such as atacamite or nantokite, as also found in [12,13]. S element is mostly present on the top corroded surface produced by the W&D test (as it was detected by XPS), as posnjakite localised crystallites, whereas on the top dropped surface, only a few Pb-S species are detected.

Moreover with both ageing methods, good agreement between the corrosion phenomena already identified for natural outdoor bronze monuments [7–10] is also confirmed, and the corrosion structure characterized by thin layers is well representative of the initial formation of natural patina. This concerns (i) the internal oxidation of the alloy marked by a decuprification process: the preferential dissolution of Cu and Zn coupled to the relative enrichment of Sn with the strong incorporation of O, (ii) the validation of the nano-porosity of the corrosion layer, confirming that patinas behave like barrier layers rather than a protective film in outdoor conditions, but also confirming the marked effect of rain run off on a bronze surface for the unsheltered areas in comparison to the sheltered areas, (iii) the specific

behaviour of chloride anions, which can be on some occasions active in the corrosion process, inducing its enrichment at the corrosion layer/alloy interface.

Thus, according to previous results reported in literature, both on ancient outdoor bronzes [7–10] and on artificially corroded surfaces [11–13], the two accelerated ageing tests proposed in this study, using an artificial rain solution with a composition similar to natural one, can be considered as very appropriate for the investigation of cultural heritage materials.

As pointed out in the introduction, the standardisation of representative aged surfaces equivalent to natural bronze patinas is a fundamental point for justifying the performance of conservation treatments, such as, for example, when designing the efficiency of protective coatings. To this aim, an implemented method in relation to artificially aged bronze patinas representative of naturally aged outdoor bronzes was developed, essential for the reproducible evaluation of conservation treatments. We also supported the idea of bringing the treatment of outdoor bronze monuments in line with regulated engineering practices. The scale up set for the dropping test device allowed the ageing of a batch of 52 samples under the same experimental conditions. However, considerations of the effect of the experimental set up initially defined in the earliest papers [12,13,15] have to be taken into account, such as the bronze composition. In particular, tin content in as-cast bronzes seems to play an important role in corrosion behaviour. As well-known for bronze alloys [16], the formation and proportion of eutectoid including delta phase is also related to the cooling rate. Thus in as-cast condition, the formation of eutectoid is observed at around 6–8 wt% Sn for industrial and artistic bronzes, quite far from the maximum Sn solubility in Cu solid solution (15.8 wt%). In this work, the Sn content of the bronze was around 7 wt%, higher than in [12,13], which was 4.4 wt%, and the presence of delta phase in the interdendritic eutectoid is quite important as evidenced from surface observation. As pointed out from FIB cross-sections, it is also revealed that delta phase is not attacked, while corrosion affects the centre of dendrites characterised by lower tin content. As also observed on ancient bronzes from different historical periods and origins [29,30], the delta phase is more stable than Cu-rich alpha phase in aerated natural environments. Even if precise investigation on the delta phase behaviour has not been performed in aqueous electrolytes, it can be mentioned that the facility of passivation decreases with the lowering of delta phase content in the eutectoid and bronze alloys with eutectoid exhibit better corrosion resistance than alpha-Cu alloys [31]. By the way, the presence of the Sn-rich δ , chemically more stable, is probably enhancing the general stability of the bronze. This could explain the less-effective corrosion impact of both the ageing tests observed in this work in comparison to the previous studies [12,13]. Furthermore,

for the dropping test, the drop dimension, the drop fall height, the average flow rate and the alternate wet and dry cycles are fundamental parameters for optimising the mechanical effect of run off. Also, the less evident erosion effect observed in this study for the dropping test in comparison to the more pronounced alteration in the reference study [12] could also be ascribed to the feebleness of impact due to the greater dimension of drops used for batch making. In this context, additional improvements could be performed for providing fully controlled ageing standards for outdoor bronze, such as including the impact of the tin concentration or the wetting condition on the corrosion rate for improving the time schedule as well as the phenomenon amplitude.

4. Conclusion

The conclusions of this work performed on quaternary bronze differently aged simulating cultural heritage monuments in outdoor conditions are as follows:

- The quaternary bronze artificial patinas produced by the dropping and W&D methods can be considered as representative aged surfaces for outdoor bronze monuments. This is a very important step towards standardisation in accordance with industrial and engineering practice, which is required for the regulation of conservation practices.
- The coupling morphology and elemental analysis of the surface and the cross-section of the artificially corroded samples allowed a fine physical and chemical characterization of the corrosion structure up to a few nm size. In particular, FIB milling on the SEM represents a promising scientific approach for bronze corrosion investigation.
- Dropping and W&D-aged bronze surfaces reveal general corrosion behaviour connected to the decuprification process, inducing internal oxidation and the preferential release of Cu and also Zn from the alloy. Both samples show layer thicknesses of a few μm in the anodic parts and few-nm-thick films in more cathodic parts, in the dendrite border close to the eutectoid. However, the corrosion layer on the samples achieved with the dropping method is more homogenous and thicker (2 μm). The corrosion layer produced by W&D highlighted a compact internal layer and porous external one of around 1 μm .
- A clear difference between the two ageing methods is the production of a slight erosion effect by the dropping and a corrosion deposit by the W&D. Mainly, the metal-oxygen compounds not well crystallised, as Cu_2O and Sn-O were observed on

the corroded surfaces by the dropping test, due to run off, whereas hydroxysulphates and cuprite characterized the patinated surface produced by the W&D test. Chlorine is found in both samples but only in very minor amounts in the anodic areas, more located within the corrosion layer for the Dropping test and at the interface of the cuprous oxide/alloy for the W&D samples.

- Nano-porosities are evidenced in both corrosion structures: uniformly distributed throughout the whole thickness for the Dropping tests, and mainly located in the external part for the W&D samples. This evidence of nano-porosities confirmed the impact of the decuprification process and can be ascribed to Cu and Zn-selective dissolution accompanied to the formation of a tin-species network within the corroded structure, forming a porous layer more evidenced in the case of rainwater run-off.

Acknowledgements

This work has been performed in the scope of the B-IMPACT project within M-ERA.NET network, supported by national funding organisations ((MIZŠ, MIUR, RMP). The authors wish to thank: Livartis d.o.o. (Slovenia) for producing quaternary alloy bronzes (www.livartis.si/en), Drs. Cédric Charvillat and Olivier Marsan, at CIRIMAT, University of Toulouse, for XRD and Raman spectroscopy measurements, respectively, and Mr. Viliem Kuhar at ZAG Institute for metallographic observations of the etched alloys.

References

- [1] A. Texier, A. A, Open air metal - outdoor metallic sculpture from the XIXth to the early XXth century, Conf. B. 2014 SF-IIC, ICOMOS, Paris. (2015) 288.
- [2] E. Cano, D. Lafuente, D.M. Bastidas, Use of EIS for the evaluation of the protective properties of coatings for metallic cultural heritage: A review, J. Solid State Electrochem. 14 (2010) 381–391. doi:10.1007/s10008-009-0902-6.
- [3] T. Kosec, A. Legat, I. Miloev, The comparison of organic protective layers on bronze and copper, Prog. Org. Coatings. 69 (2010) 199–206. doi:10.1016/j.porgcoat.2010.04.010.
- [4] C. Chiavari, E. Bernardi, D. Cauzzi, S. Volta, M.C. Bignozzi, B. Lenza, et al., Influence of natural patinas of outdoor quaternary bronzes on conservation treatments, Met. 2013 Proc. Interim Meet. ICOM-CC Met. Work. Gr. (2013) 159–168.
- [5] T. Kosec, H. Otmacic Curkovic, A. Legat, Investigation of the corrosion protection of

- chemically and electrochemically formed patinas on recent bronze, *Electrochim. Acta*. 56 (2010) 722–731. doi:10.1016/j.electacta.2010.09.093.
- [6] P. Eriksson, L.-G. Johansson, J. Gullman, A laboratory study of corrosion reactions on statue bronze, *Corros. Sci.* 34 (1993) 1083–1097. doi:http://dx.doi.org/10.1016/0010-938X(93)90290-W.
- [7] L. Robbiola, H.P. Hurtel, Nouvelle contribution à l'étude des mécanismes de corrosion des bronzes de plein air: caractérisation de l'altération de bronzes de Rodin, (1991) 809–823.
- [8] C. Chiavari, K. Rahmouni, H. Takenouti, S. Joiret, P. Vermaut, L. Robbiola, Composition and electrochemical properties of natural patinas of outdoor bronze monuments, *Electrochim. Acta*. 52 (2007) 7760–7769. doi:10.1016/j.electacta.2006.12.053.
- [9] L. Robbiola, C. Fiaud, S. Pennec, New model of outdoor bronze corrosion and its implications for conservation, in: *ICOM Comm. Conserv. Tenth Trienn. Meet.*, August 199, Washington DC, USA, 1993: pp. 796–802.
- [10] L. Robbiola, K. Rahmouni, C. Chiavari, C. Martini, D. Prandstraller, A. Texier, et al., New insight into the nature and properties of pale green surfaces of outdoor bronze monuments, *Appl. Phys. A Mater. Sci. Process.* 92 (2008) 161–169. doi:10.1007/s00339-008-4468-4.
- [11] S. Goidanich, I.O. Wallinder, G. Herting, C. Leygraf, Corrosion induced metal release from copper based alloys compared to their pure elements, *Corros. Eng. Sci. Technol.* 43 (2008) 134–141. doi:10.1179/174327808X286383.
- [12] E. Bernardi, C. Chiavari, B. Lenza, C. Martini, L. Morselli, F. Ospitali, et al., The atmospheric corrosion of quaternary bronzes: The leaching action of acid rain, *Corros. Sci.* 51 (2009) 159–170. doi:10.1016/j.corsci.2008.10.008.
- [13] C. Chiavari, E. Bernardi, C. Martini, F. Passarini, F. Ospitali, L. Robbiola, The atmospheric corrosion of quaternary bronzes: The action of stagnant rain water, *Corros. Sci.* 52 (2010) 3002–3010. doi:10.1016/j.corsci.2010.05.013.
- [14] M.L. Young, S. Schnepf, F. Casadio, A. Lins, M. Meighan, J.B. Lambert, et al., Matisse to Picasso : a compositional study of modern bronze sculptures, (2009) 171–184. doi:10.1007/s00216-009-2938-y.
- [15] C. Chiavari, E. Bernardi, A. Balbo, C. Monticelli, S. Raffo, M.C. Bignozzi, et al., Atmospheric corrosion of fire-gilded bronze: corrosion and corrosion protection during accelerated ageing tests, *Corros. Sci.* 100 (2015) 435–447.

doi:<http://dx.doi.org/10.1016/j.corsci.2015.080.013>.

- [16] R.N. Caron, R.G. Barth, D.E. Tyler, Metallography and Microstructures of copper and its alloys, in: *Metallogr. Microstruct.* Vol 9, ASM Handb., ASM International, 2004: pp. 775–788.
- [17] A. Krätschmer, I. Odnevall Wallinder, C. Leygraf, The evolution of outdoor copper patina, *Corros. Sci.* 44 (2002) 425–450. doi:10.1016/S0010-938X(01)00081-6.
- [18] I. Odnevall Wallinder, C. Leygraf, A study of copper runoff in an urban atmosphere, *Corros. Sci.* 39 (1997) 2039–2052.
- [19] F. Ospitali, C. Chiavari, C. Martini, E. Bernardi, F. Passarini, L. Robbiola, The characterization of Sn-based corrosion products in ancient bronzes: A Raman approach, *J. Raman Spectrosc.* 43 (2012) 1596–1603. doi:10.1002/jrs.4037.
- [20] V. Hayez, V. Costa, J. Guillaume, A. Hubin, Micro Raman spectroscopy used for the study of corrosion products on copper alloys : study of the chemical composition of artificial patinas used for restoration purposes, *Analyst.* 130 (2005) 550–556. doi:10.1039/b419080g.
- [21] M.C. Bernard, S. Joiret, Understanding corrosion of ancient metals for the conservation of cultural heritage, *Electrochim. Acta.* 54 (2009) 5199–5205. doi:10.1016/j.electacta.2009.01.036.
- [22] P. Colomban, A. Tournié, M. Maucuer, P. Meynard, On-site Raman and XRF analysis of Japanese/Chinese bronze/brass patina – the search for specific Raman signatures, *J. Raman Spectrosc.* 43 (2012) 799–808. doi:10.1002/jrs.3095.
- [23] S.K. Chawla, N. Sankarraman, J.H. Payer, Diagnostic Spectra for XPS analysis of Cu-O-S-H compounds.pdf, *J. Electron Spectros. Relat. Phenomena.* 61 (1992) 1–18.
- [24] V. Hayez, A. Franquet, A. Hubin, H. Terryn, XPS study of the atmospheric corrosion of copper alloys of archaeological interest, *Surf. Interface Anal.* 36 (2004) 876–879. doi:10.1002/sia.1790.
- [25] M.C. Squarzialupi, G.P. Bernardini, V. Faso, A. Atrei, G. Rovida, Characterisation by XPS of the corrosion patina formed on bronze surfaces, *J. Cult. Herit.* 3 (2002) 199–204. doi:10.1016/S1296-2074(02)01179-2.
- [26] M. Chan, A. Capek, D.A. Brill, S.J. Garrett, Characterization of the patina formed on a low tin bronze exposed to aqueous hydrogen sulfide, *Surf. Interface Anal.* 46 (2014) 433–441. doi:10.1002/sia.5520.
- [27] L. Robbiola, J.M. Blengino, C. Fiaud, Morphology and mechanisms of formation of natural patinas on archeological Cu-Sn alloys, *Corros. Sci.* 40 (1998) 2083–2111.

- [28] L. Robbiola, T.T.M. Tran, P. Dubot, O. Majerus, K. Rahmouni, Characterisation of anodic layers on Cu-10Sn bronze (RDE) in aerated NaCl solution, *Corros. Sci.* 50 (2008) 2205–2215. doi:10.1016/j.corsci.2008.06.003.
- [29] N. Meeks, Surface characterization of tinned bronze, high-tin bronze, tinned iron and arsenical bronze, in: *Met. Plat. Patination; Cult. Tech. Hist. Dev.*, Butterworth–Heinemann, 1993: pp. 247–275.
- [30] M. Taube, A.H. King, W.T. Chase, Transformation of ancient Chinese and model two-phase bronze surfaces to smooth adherent patinas, *Phase Transitions*. 81 (2008) 217–232. doi:10.1080/01411590701514375.
- [31] A.M. Shams El Din, F.M. Abd El Wahab, The Behaviour of copper-tin alloys in alkaline solutions upon alternate anodic and cathodic polarization, *Electrochim. Acta*. 10 (1965) 1127–1140. doi:http://dx.doi.org/10.1016/0013-4686(65)80037-8.

Figure captions

Figure 1: (a) Schematic mode for a large-scale production of dropping test samples and (b) general view of the dropping system; (c) detail showing the quaternary bronze samples (at 45°) during ageing exposed at 45°.

Figure 2: Optical examination of as-cast quaternary alloy before corrosion (tint etchant Klemm III): (a) as-cast alloy with large dendritic structure (mm size); (b) cross-section with vertical preferential orientation of the dendrites linked to cooling temperature gradient from the top surface to the plate centre; corroded surfaces obtained by dropping (D) and by wet & dry (W&D): (c-d) Optical bright-field observation and (e-f) 3-D digital microscopy topographic images of bronze samples after artificial corrosion by the dropping and W&D tests, respectively.

Figure 3: SEM observation and X-ray intensity maps of surface aged by dropping (a-c) and W&D (d-f): (a) and (d) BSE images; (b) and (e) Composite X-ray map image (O in green, Cu in magenta and Sn in blue) showing that the corrosion mainly affects the dendrite centre; (c) Composite X-ray map image (Cl in green and Cu in red) revealing a higher Cl concentration in the centre of corroded dendrite; (f) Composite X-ray map image (S in red and Cl in green) showing a large amount of S in the dendrite linked to the corrosion deposit.

Figure 4: Grazing-angle X-ray diffraction (GXRD) of the corroded surface by (a) dropping and (b) W&D; Raman spectroscopy performed on corroded dendrite of artificial quaternary bronze patinated surface by (c) dropping (top spectrum: metal-O stretching vibration / bottom spectrum: cuprous oxide) and by (d) W&D (top: posnjakite / bottom: cuprous oxide).

Figure 5: XPS surveys of the corroded surfaces by dropping and W&D before and after Ar⁺ ion etching.

Figure 6: XPS core levels of O 1s, Cu 2p and S 2p curve fitted regions, after Ar⁺-ion etching, on the bronze surface corroded by dropping (a, c and e, respectively) and W&D (b, d, f, respectively).

Figure 7: Images of the corroded surface and cross-sections prepared by FIB milling of samples obtained by Dropping and W&D: (a) and (b) surface areas corresponding to cross-section obtained by FIB milling; (c) and (d) general views of the cross-section after FIB milling (rectangles are corresponding to details shown in Figure 8).

Figure 8: Cross-sections prepared by FIB milling of samples obtained by dropping and W&D, corresponding to areas defined in Figure 7c-d: (A) dendrite centre, (B) dendrite borders corresponding to the transition corroded dendrite / eutectoid area and (C) interdendritic space (eutectoid).

Figure 9: High-magnification observation of the corrosion layer revealing the porosity of bronze patinas on a nanometre scale obtained with FIB cross-sections of (a) the dropping and (b) the W&D samples.

Figure 10: Representative EDS line-scan profiles of the quaternary alloy, located on the bulk alloy parallel to the corrosion layer and centred on the corroded dendrite.

Figure 11: X-ray maps of the corrosion layer produced by W&D test in the centre of dendrite obtained by FIB cross-section (A right-hand image of Figure 8).

Figure 12: Elemental line profiles (X-ray intensity vs distance) obtained by cross-section prepared by FIB milling within the corrosion layer produced by dropping: (a) centre of corroded dendrite, and by W&D: (b) thicker part of the corroded dendrite and (c) thin layer in the dendrite border.

Tables

Table 1: Chemical composition of quaternary bronze artificially patinated through dropping and W&D (EDS – Beam energy 15 kV). The reported results are an average obtained from different areas.

at%	O	S	Cl	Cu	Zn	Sn	Pb	Cu/Sn
<i>Dendrite border close to eutectoid</i>								
Dropping	11±4	-	-	80±4.0	2.6±0.2	6.6±0.3	0.1±0.1	12.1
W&D	14.7±0.5	-	-	76.4±0.3	2.3±0.1	6.5±0.1	-	11.8
<i>corroded dendrite : external part</i>								
Dropping	60±1	0.1±0.1	0.3±0.1	31±2	0.6±0.1	7.5±0.7	0.2±0.1	4.1
W&D	54±3	0.8±0.1	0.7±0.1	37±3	0.4±0.1	7.1±0.1	0.7±0.1	5.2
<i>corroded dendrite: central part</i>								
Dropping	48±3	0.2±0.1	-	46±4	1.1±0.3	4.5±0.4	0.2±0.1	10
W&D	39±5	0.6±0.1	1.0±0.3	55±5	0.9±0.4	3.6±0.4	0.4±0.1	15.3

Table 2: XPS atomic quantification on corroded surface by Dropping and W&D before and after Ar⁺-ion etching.

	Cu 2p _{3/2}	Sn 3d _{5/2} Sn(IV)	Zn 2p _{3/2} oxide	Pb 4f _{7/2} Pb(II)	C 1s CC, CH/C-O/O-C=O	O 1s	S 2p S- metal/sulfate
<i>Before etching</i>							
Dropping							
<i>Peak BE (eV)</i>	934.7	486.8	1022.2	138.6	284.9/286.5/288.4	531.8	161.8/167.8
<i>at%</i>	5.6	5.1	0.1	0.4	25.0/10.2/11.9	40.9	0.3/0.5
W&D							
<i>Peak BE (eV)</i>	935.2	486.7	-	138.6	284.5/286.2/288.0	531.7	163.0/168.5
<i>at%</i>	8.6	0.7	-	0.2	34.8/7.1/4.3	35.5	0.3/8.5
<i>After etching</i>							
Dropping							
<i>Peak BE (eV)</i>	933.2	486.8	1022.1	138.5	284.8/286.4/288.4	531.3	162.1/167.9
<i>at%</i>	16.9	10.7	0.5	0.8	17.7/4.5/4.6	43.4	0.5/0.4
W&D							
<i>Peak BE (eV)</i>	933.3	486.7	-	138.6	284.5/286.2/288.0	531.7	163.0/168.5
<i>at%</i>	11.8	1.3	-	0.3	37.1/4.9/3.6	31.3	1.8/7.9

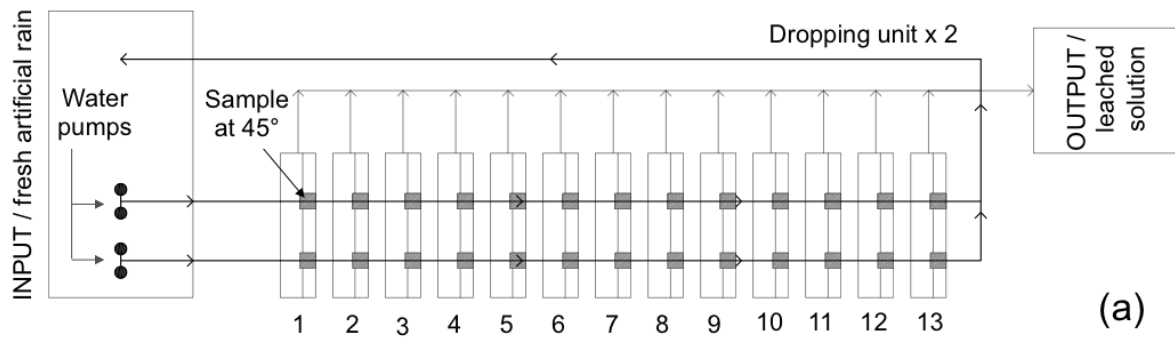


Figure 1

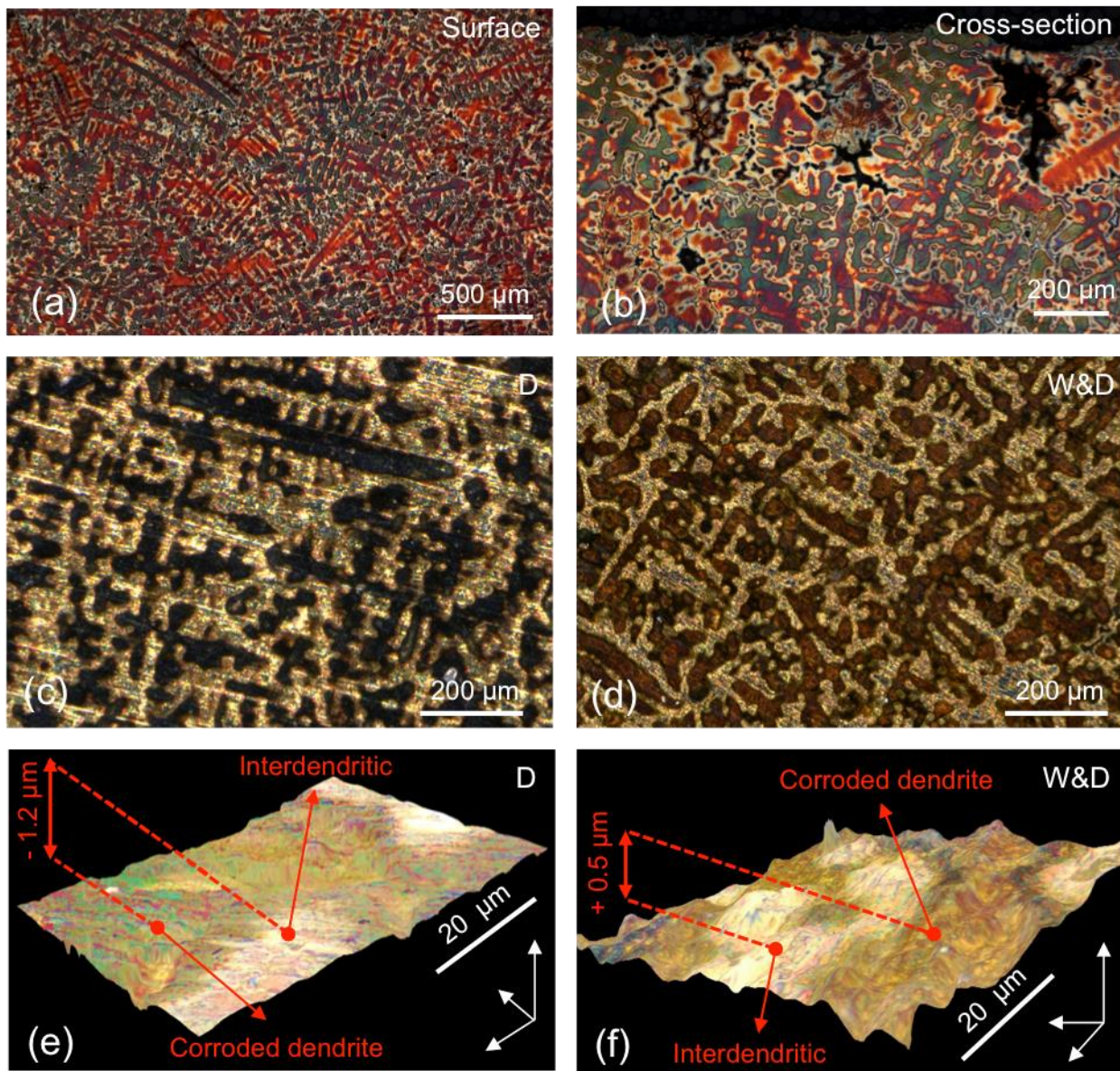


Figure 2

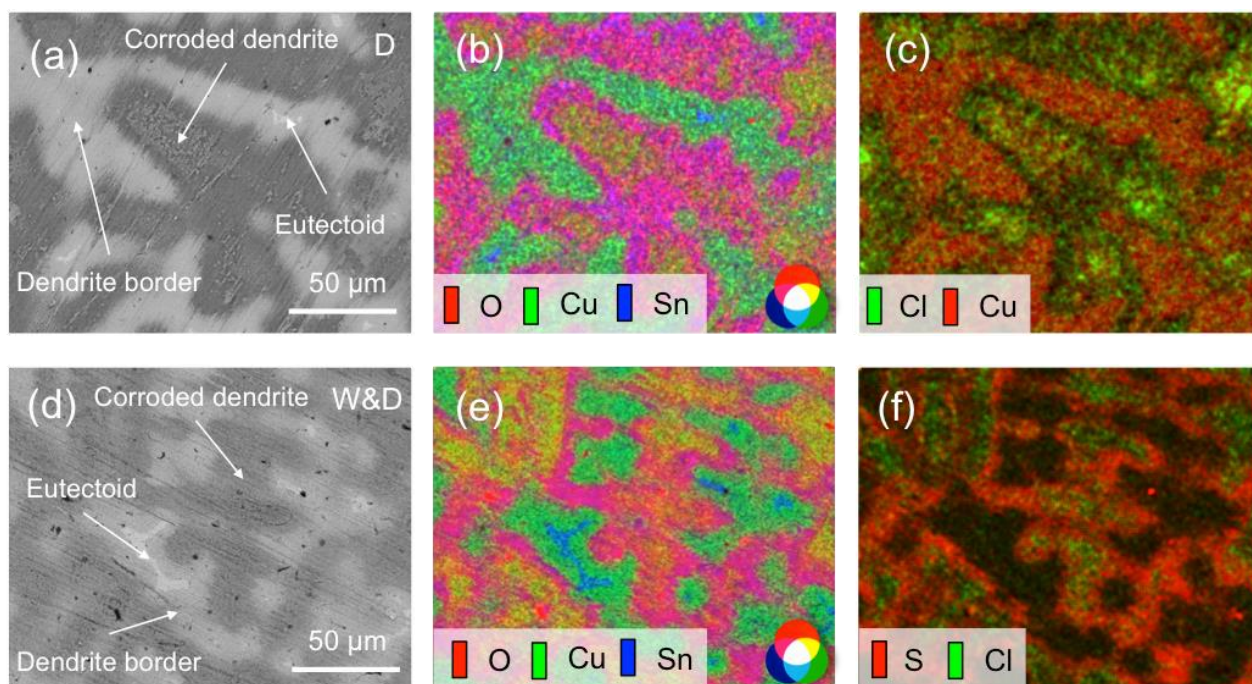


Figure 3

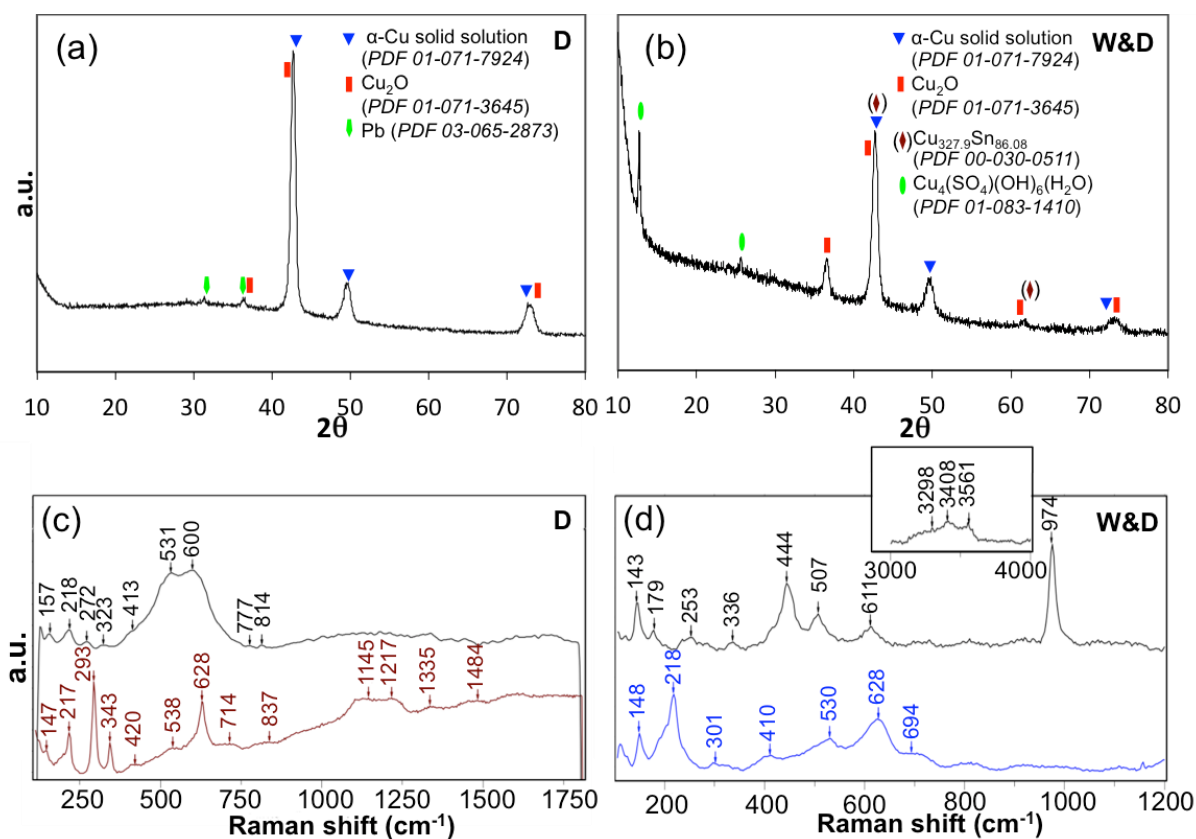


Figure 4

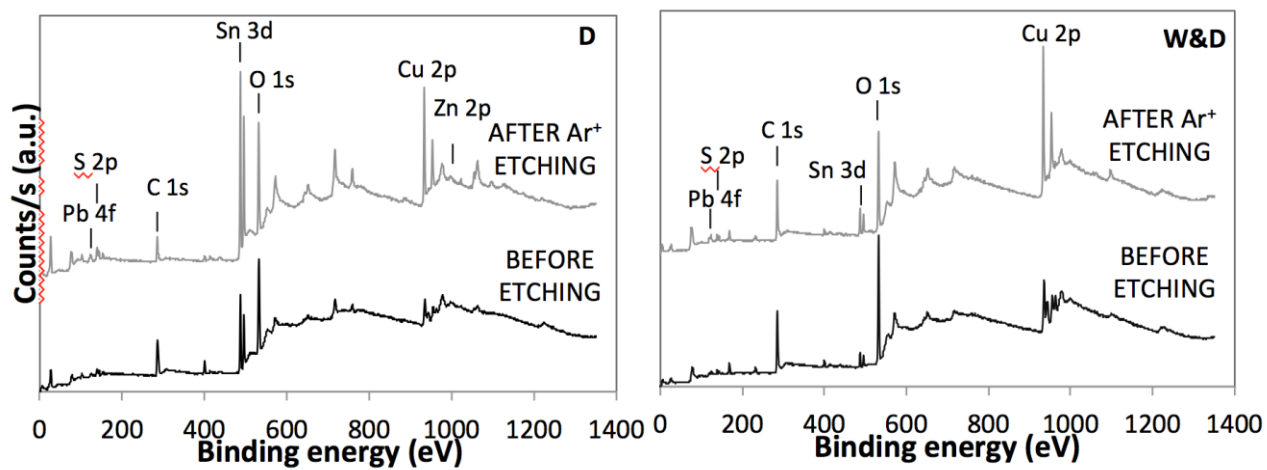


Figure 5

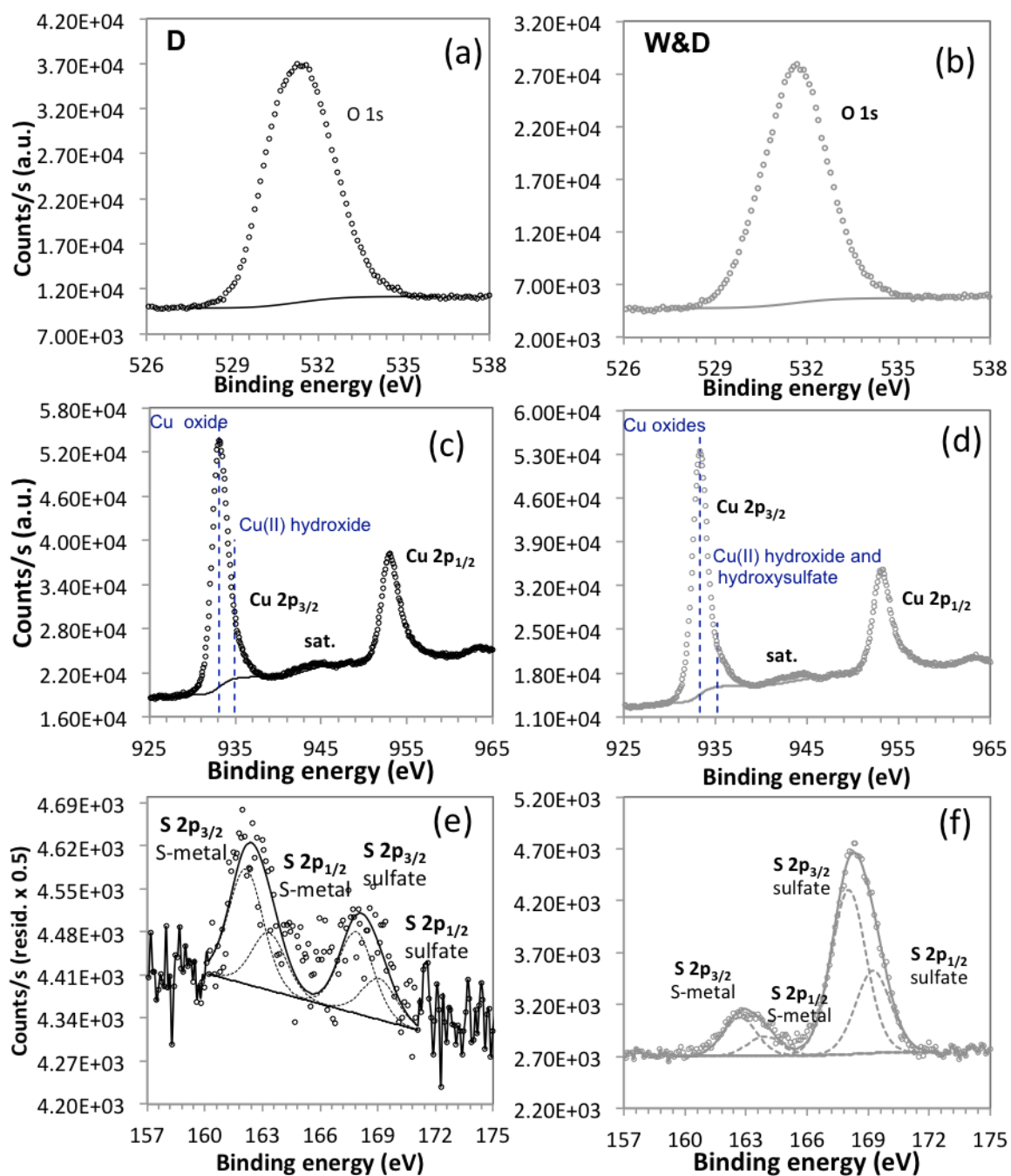


Figure 6

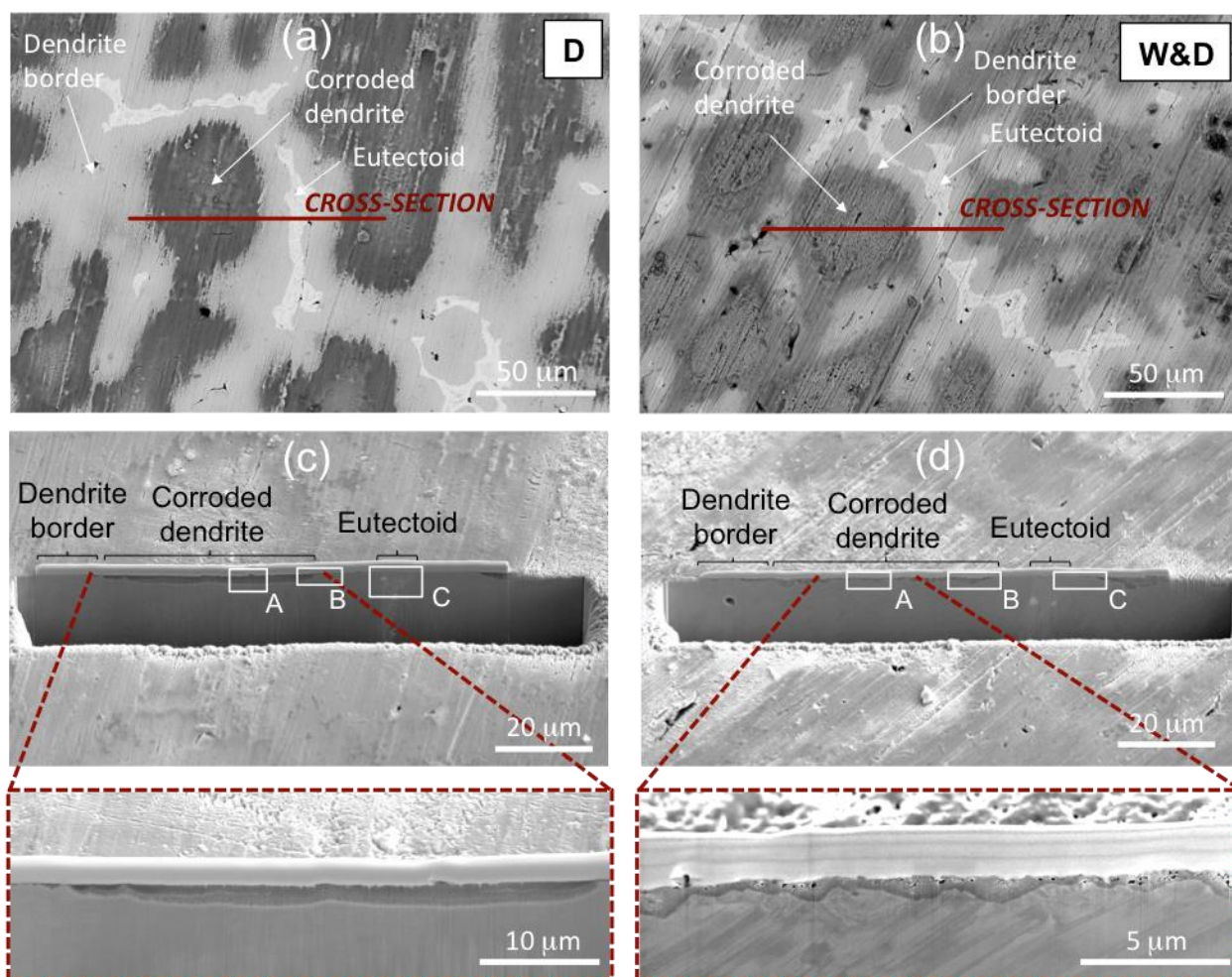


Figure 7

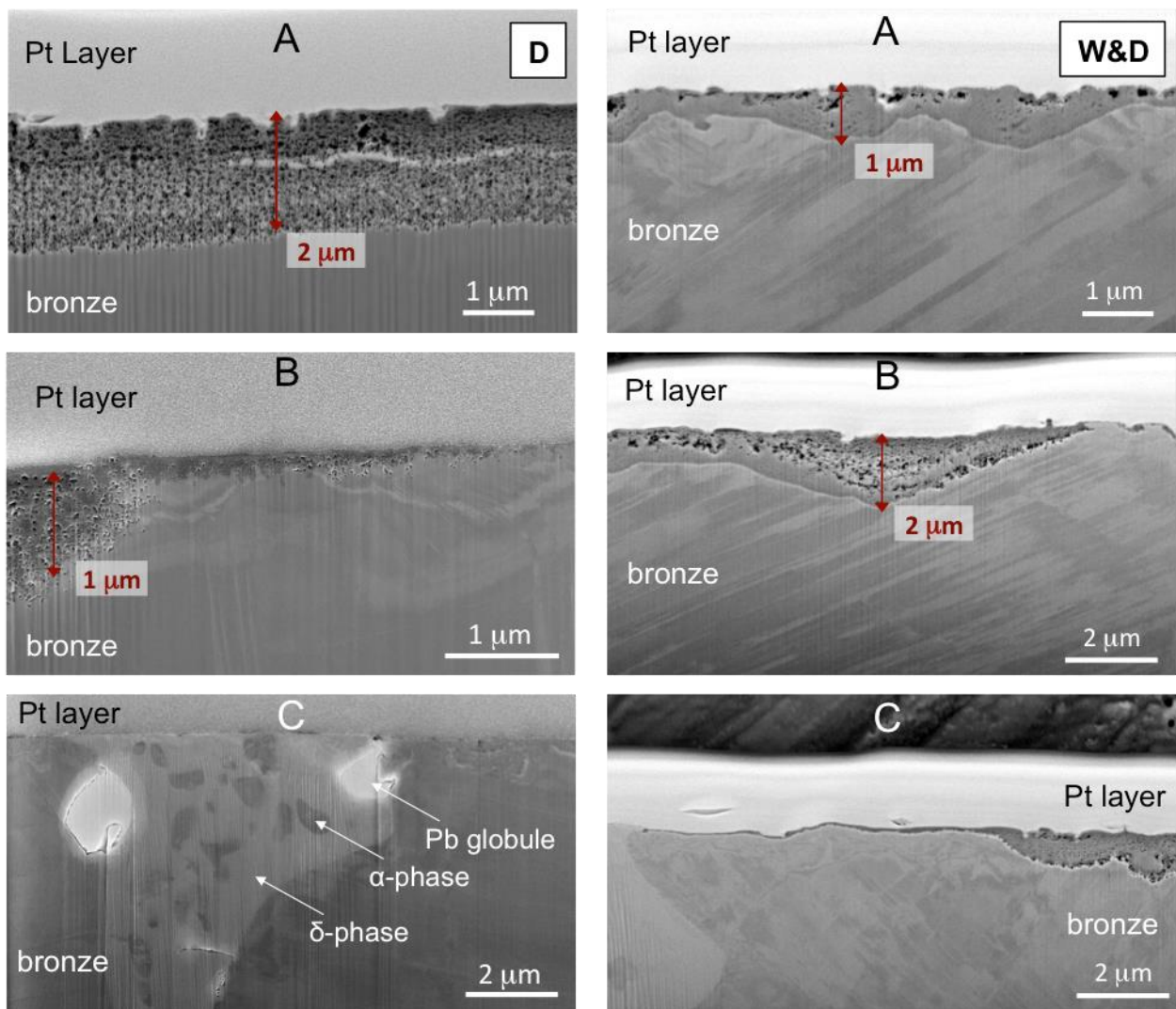


Figure 8

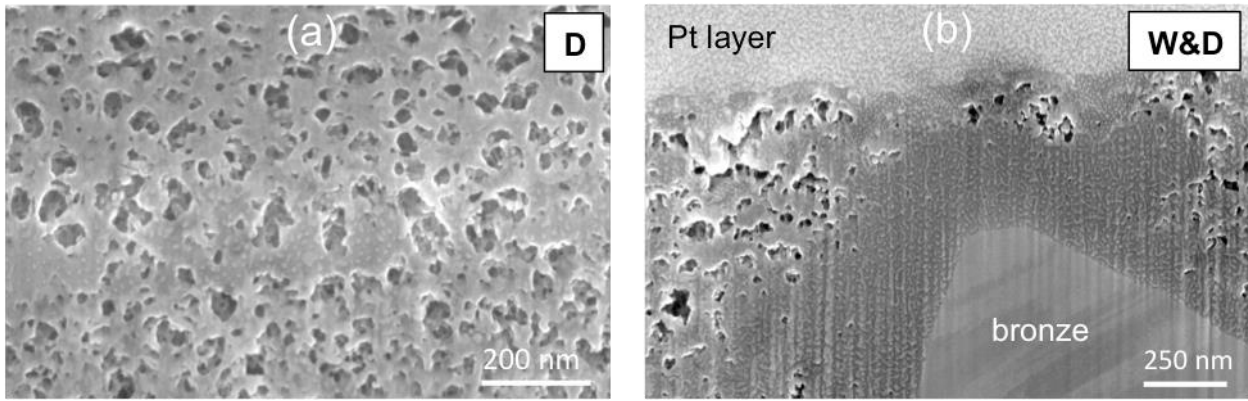


Figure 9

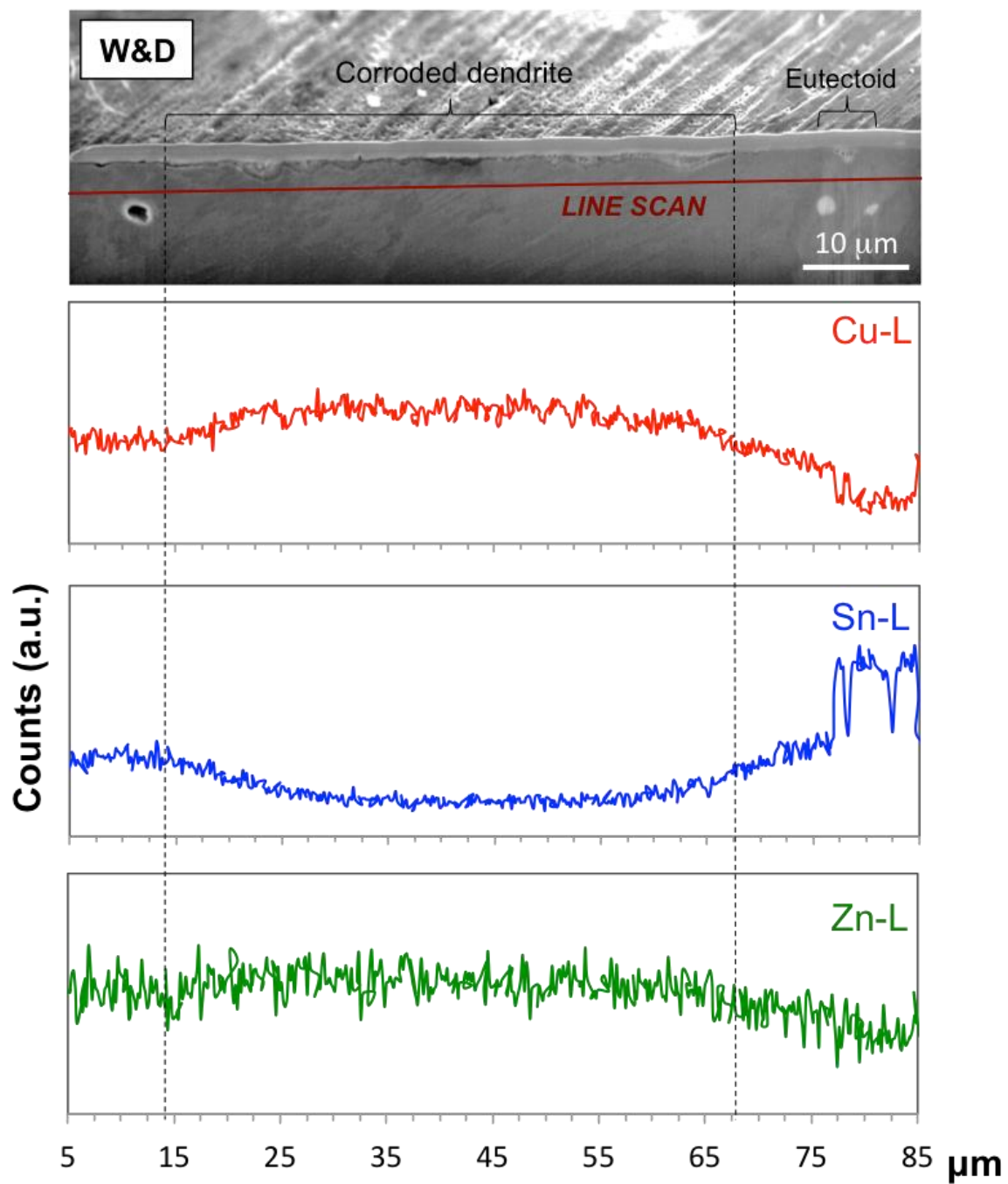


Figure 10

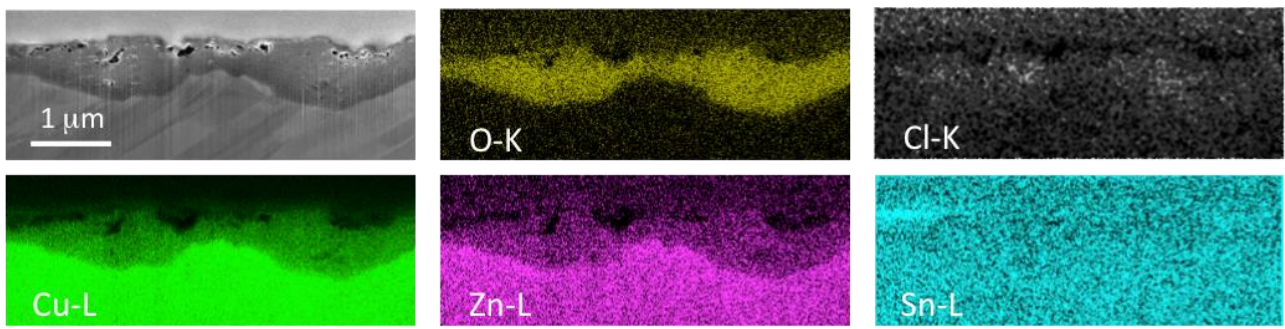


Figure 11

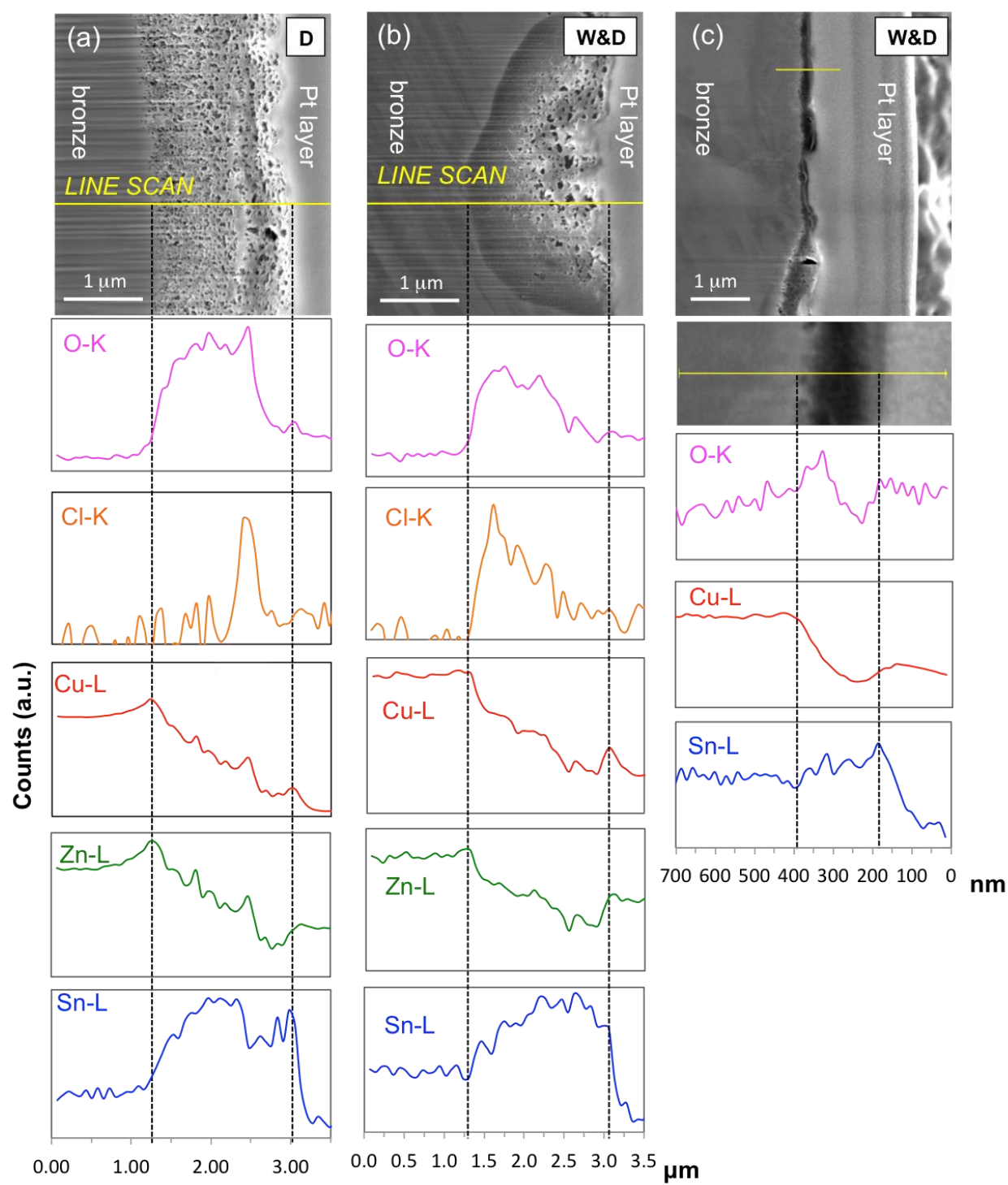


Figure 12